Journal of Thermal Analysis and Calorimetry
https://doi.org/10.1007/s10973-025-14693-9

Exact multiple solutions for rheological analysis of Darcy–Brinkman model on Bingham sodium alginate suspensions driven by 2D bidirectional moving plate with Navier and Biot conditions

S. M. Sachhin[1] · U. S. Mahabaleshwar[1] · David Laroze[2] · L. M. Pérez[3]

Received: 2 January 2025 / Accepted: 10 August 2025

Abstract
In modern days, Bingham ternary nanofluid applications gain the attention of many researchers with their unique properties and potential applications in solar thermal energy conversion which significantly improve system efficiency and leverage modern machine learning techniques for performance prediction, and the authors observe that there is a dearth of research on Bingham ternary nanofluids with the circumstance of momentum slip and temperature jump conditions and influence of MHD (magnetohydrodynamics) and thermal radiation on ternary nanofluids; authors utilized the research gap and used GO, MoS_2, and TiO_2 nanoparticles mixed in sodium alginate solution to form non-Newtonian Bingham ternary nanofluid. Further, the heat transfer process was analyzed using variable thermophysical properties, momentum, and temperature-governing equations, which were transformed to nonlinear ordinary differential equations (ODEs) via similarity variables. The temperature equation was calculated using the hypergeometric series method, and several physical parameters are explained graphically. The outcomes reveal that upsurging the porous, magnetic field, and slip parameters decays the momentum profile, and enhancing the thickness of the thermal boundary layer, the present analysis has many useful applications in science and engineering industries, such as transportation, cooling systems, and heat exchangers.

Keywords Ternary nanofluids · Bingham fluid · Brinkman ratio · Heat transfer · Biot number

Abbreviations

HNF	Hybrid nanofluid
B. Cs	Boundary conditions
MHD	Magnetohydrodynamics
PDE	Partial differential equation
ODE	Ordinary differential equation

List of symbols

$A_1\,A_2\,A_3\,A_4\,A_5$	Constants
a	Acceleration rate
H_0	Magnetic strength
Cp	Specific heat
Da^{-1}	Inverse Darcy number
d	Stretching /shrinking parameter
f	Velocity function
Nr	Radiation
Pr	Prandtl number
qr	Radiative heat flux
S	Mass suction/injection
T	Temperature of the fluid
T_w	Temperature of the surface
T_∞	Ambient temperature
u, v	x, y-Axis velocity components
u_w	Velocity
x, y	Axis

Greek symbols

δ	Solution term
η	Similarity variable
κ	Thermal conductivity

✉ U. S. Mahabaleshwar
u.s.m@davangereuniversity.ac.in

✉ L. M. Pérez
lperez@academicos.uta.cl

S. M. Sachhin
sachinsm030@gmail.com

David Laroze
dlarozen@uta.cl

[1] Department of Studies in Mathematics, Shivagangothri, Davangere University, Davangere, India

[2] Instituto de Alta Investigación, Universidad de Tarapacá, Casilla 7 D, 1000000 Arica, Chile

[3] Departamento de Ingeniería Industrial y de Sistemas, Universidad de Tarapacá, Casilla 7D, 1000000 Arica, Chile

Published online: 24 October 2025

k^*	Absorption coefficient
μ	Dynamic viscosity
ν	Kinematic viscosity
ρ	Fluid density
ψ	Stream function
σ	Electrical conductivity
σ^*	Stephen–Boltzmann constant
θ	Non-dimensional temperature

Introduction

Non-Newtonian fluids have gained essential attention from scientists and engineers in recent years with their wide range of uses in energy and technology fields. Non-Newtonian fluids can be found in everyday products such as cosmetics, paper production, fiber technology, ketchup, paint, shampoo, blood, lubricants, and plastic. However, due to their unique behavior under shear stress, a single relation cannot predict all non-Newtonian fluids. Ramzan et al. [1] studied ternary nanofluid flow influenced by magnetohydrodynamics with entropy generation. Ternary nanofluid flows over a widening surface with induction impacts studied by Alharbi [2] and Sahoo [3]. Numerical method was used by Sachhin [4] to study the heat transfer and radiation effect on the fluid flow. [5] explored the heat generation on nanofluid flow on the Fourier heat flux model.

An exact solution for modeling of nanofluid flow across permeable stretching surface using heterogeneous solutions is studied by Datta et al., [6]. Bernard [7] studied the saturation of trapped gas on the permeable water medium with the impact of foam. Effect of solar radiation and mass suction/suction is studied by Akshatha [8] on the nanofluid flow across the stretchable sheet. Vafai et al., [9] studied the thermal transfer at the boundary by the two regions across the permeable surface using analytical techniques. Ochoa et al., [10] and Haga [11] explored the theoretical framework for understanding the transfer of momentum at the boundary permeable media with the pressure oscillations.

Mass transfer plays a vital role in fluid flow, particularly in processes like drying, distillation, and chemical reactions. It influences concentration gradients, which can affect fluid behavior and mixing efficiency. Understanding this interaction is essential for optimizing industrial operations and improving system performance. Choi [12] and Huminic [13] examined the entropy generation on the fluid flow with heat and mass transfer. Afterward, Das [14] discovered the impact of heat transfer in both conventional and ternary nanofluids with a comprehensive review. Suresh [15] and Siddiqui [16] explored the stability and mass transfer of hybrid nanoliquid flow with pressure drop characteristics. Analytical methods utilized by Sachhin et al., [17] to solve the energy equations using boundary conditions. Rostami [18] used artificial neural networks to study the measurement of heat conductivity on hybrid nanoliquid flow.

Nanofluids, which are fluids containing nanoparticles, increase the thermal conductivity and heat transfer properties of base fluids. Their use in fluid flow systems improves cooling performance in applications like electronics, automotive engines, and solar collectors. This leads to more efficient thermal management and energy savings. Nisa [19] studied the Brinkman model of fractional convection movement of a hybrid nanoliquid on an inclined surface. Afterward, analytical methods were used by Sene [20] and Abed [21] to explore the nonlinear stability analysis on the Brinkman-type fluid flow via a rotating cylinder using symmetric properties. Safa [22] and [23, 24] scrutinized the effect of aerosol nanoparticles bounded by the Brinkman medium. Devi et al., [25] examined the binary nanofluid movement on an expanding surface with stability analysis using the Darcy model. Many researchers studied the influences of energy and mass transfer on nanofluid flows across various geometries using nanoparticles such as [26–38].

Thermal radiation significantly influences fluid flow, especially in high-temperature environments such as combustion chambers and space applications. It affects heat transfer rates, altering fluid temperature and velocity profiles. This interaction is crucial in designing thermal systems and improving energy efficiency. Souayeh [39] examined the Nusselt number and thermal conductivity impact on natural convective fluid flow across rectangular conductive surface. Bezi [40] studied the heat transfer impact on ternary nanofluid movement across half-annulus surface. Hdhiri [41] explored the Nusselt number and porous media impact on fluid flow by using finite volume method. Souayeh [42, 43] examined the heat transfer influence on non-Newtonian fluid flow over various surfaces. Nuwairan [44] explored the magnetic field and thermophoresis influence on non-Newtonian fluid flow over expanding surface, and Waseem [45] explored the radiation and heat source influence on micropolar fluid flow over stretchable sheet. Lone [46] studied the entropy analysis impact on mixed convective hybrid nanofluid flow across stagnated surface. Awati [47] explored the chemical reaction impact on Williamson fluid flow across stagnation point using numerical method. Lone [48] studied the activation energy impact on bio-convective fluid flow across expanding surface.

Inspired by the abovementioned studies and applications, the authors point out that there is a dearth of studies on non-Newtonian fluids with the circumstance of Navier's slip and temperature jump conditions and impacts of MHD and solar radiation on ternary nanofluids and utilized the research gap and studied the influence of MHD and the Brinkman ratio on biviscous Bingham ternary nanoliquid flow with heat source and solar radiation across stretching/shrinking sheet with Navier's slip and

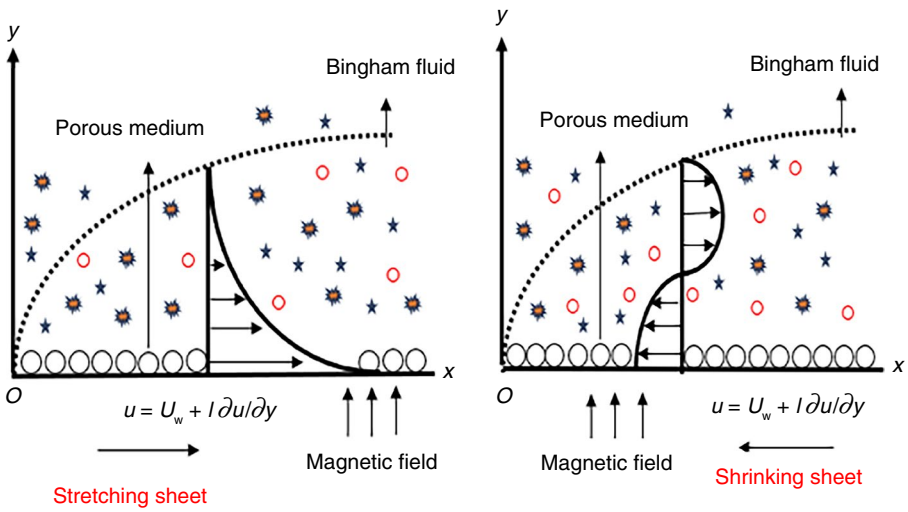

Fig. 1 Schematic representation of flow boundary

Table 1 Nanoparticle physical properties [26, 27]

Properties	SA	MoS_2	GO	TiO_2
σ/Sm^{-1}	2.6×10^{-4}	0.01	4.57×10^{-6}	10^{-10}
ρ/kgm^{-3}	989	5.06×10^{3}	1800	4250
Cp/JkgK^{-1}	4175	397.21	717	686.20
κ / W $\mathrm{m}^{-1}\mathrm{K}^{-1}$	0.6376	34.5	5000	8.9538
Volume fraction values		$\phi_1 = 0.01$	$\phi_2 = 0.01$	$\phi_3 = 0.01$

temperature jump. The famous analytic hypergeometric method is used to solve the energy equation, and adding an MHD produces a current in a flowing conductive liquid which produces forces on the liquid; current analysis has many uses in biomedical and engineering fields. Figure 1 represents the schematic diagram, and Tables 1 and 2 represent the thermophysical properties and comparison of analytical results with previously published studies.

Governing equations

Consider an MHD and heat source with the permeable surface in a Bingham ternary nanofluid movement over an expanding/shrinking sheet. Considering the flow as laminar and incompressible, magnetic field applied normal to the sheet, thermal radiation and heat source effects are considered in energy distribution, u and v are the velocities along x- and y-axis, T represents the temperature, velocity slip, and Biot boundary conditions are considered. Figure 1 portrays the schematic representation of the fluid flow, and the assumptions of fluid movement are as follows:

- Fluid movement is created by stretching and contracting the surface; therefore, there does not exist a pressure gradient impacting the flow, i.e., $\nabla p = 0$.
- Examined the steady-state problem, i.e., $\frac{\partial u}{\partial t} = 0$ and laminar flow
- Deduced valid boundary layer approximations (Prandtl (1904)) as follows:

(i) The velocity of the fluid in the axial direction is greater than the transverse direction, i.e., $u \gg v$.
(ii) Variations of axial velocity are much more than the transverse velocity.
(iii) Assuming a stretching velocity (see Crane [36]).

Table 2 Similar analytical study comparison with other authors

Related works by other authors	Fluids	Value of momentum solution
Crane [36]	Newtonian	$\delta = 1$
Khan [28]	Non-Newtonian	$f(\eta) = f_w + \frac{\lambda}{\delta}(1 - \exp[-\delta\eta])$, $\delta = \frac{3f_w\left(\frac{\rho_{hnf}}{\rho_f}\right) \pm \sqrt{9f_w^2\left(\frac{\rho_{hnf}}{\rho_f}\right)^2 + 4\left(\frac{\mu_{hnf}}{\mu_f}\right)3\lambda\left(\frac{\rho_{hnf}}{\rho_f}\right) + \left(\frac{\sigma_{hnf}}{\sigma_f}\right)M}}{2\left(\frac{\mu_{hnf}}{\mu_f}\right)}$,
Hamid [26]	Newtonian	$f(\eta) = s + \frac{\alpha}{\delta(1+b\delta)}\left(1 - e^{-\delta\eta}\right)$ $(2+\lambda)b\delta^3 + (2 + 2\lambda - 2bs)\delta^2 - 2s\delta - 2a = 0$,
Present work	Non-Newtonian	$f(\eta) = S + d\frac{(1-e^{-\delta\eta})}{(\delta+b\delta^2)}$ $\Lambda\left(1+\frac{1}{\Gamma}\right)b\delta^3 + \left[\Lambda\left(1+\frac{1}{\Gamma}\right) - A_2Sb\right]\delta^2 - \left(A_3Qb + A_1Da^{-1}b - A_2S\right)\delta$ $-\left(A_3Q + A_1Da^{-1} + A_2d\right) = 0$

Navier [38] proposed the component of velocity slip condition as follows:

$$u = l\frac{\partial u}{\partial y}. \tag{1}$$

Consider the rheological characteristics of biviscosity Bingham fluid as follows [25]:

$$\tau_{ij} = \begin{cases} 2(\mu_B + p_y/\sqrt{2\pi})e_{ij}, & \pi > \pi_c, \\ 2(\mu_B + p_y/\sqrt{2\pi_c})e_{ij}, & \pi < \pi_c, \end{cases} \tag{2}$$

where P_y is written as

$$P_y = \frac{\mu_b\sqrt{2\pi_c}}{\Gamma}, \tag{3}$$

where π and π_c are the deformation rate product and product value, and P_y and μ_B are yields stress and viscosity of plastic deformation.

The principle of conservation mass [26, 28] is as follows:

$$\nabla \cdot \vec{q} = 0; \tag{4}$$

the conversation of linear momentum [26, 28] is as follows:

$$\left[\vec{q}_t + \left(\vec{q}\cdot\nabla\right)\vec{q}\right] = -\frac{\nabla p}{\rho_{tnf}} + \frac{\mu_{eff}}{\rho_{tnf}}\left(1 + \frac{1}{\Gamma}\right)\nabla^2\vec{q} - \left(\frac{\mu_{tnf}}{\rho_{tnf}K_1} + \frac{\sigma_{tnf}H_0^2}{\rho_{tnf}}\right)\vec{q}, \tag{5}$$

And the governing equations are as follows [26, 28]:

$$\frac{\partial u}{\partial x} + \frac{\partial v}{\partial y} = 0, \tag{6}$$

$$u\frac{\partial u}{\partial x} + v\frac{\partial u}{\partial y} = \frac{\mu_{eff}}{\rho_{tnf}}\left(1 + \frac{1}{\Gamma}\right)\frac{\partial^2 u}{\partial y^2} - \frac{\sigma_{tnf}}{\rho_{tnf}}H_0^2 u - \frac{\nu_{tnf}}{K_1}u, \tag{7}$$

$$u\frac{\partial T}{\partial x} + v\frac{\partial T}{\partial y} = \frac{\kappa_{tnf}}{(\rho Cp)_{tnf}}\frac{\partial^2 T}{\partial y^2} - \frac{1}{(\rho Cp)_{tnf}}\frac{\partial qr}{\partial y} + \frac{Q_0(T - T_\infty)}{(\rho Cp)_{tnf}}, \tag{8}$$

B. Cs are given by [26]

$$u = U_w(x) + l\frac{\partial u}{\partial y},\ v = v_w,\ -k\frac{\partial T}{\partial y} = h(T_w - T), \quad \text{as } y \to 0,\ u = 0,\ T = T_\infty,\ \text{at } y \to \infty. \tag{9}$$

where u and v are velocities along the x- and y-axis, and ν, κ, ρ, andσ are the dynamic viscosity, thermal conductivity, density, and electrical conductivity, respectively. H_0 is the magnetic field strength, K_1 is the permeability, and T denotes the energy of the fluid. Introducing the converted form of PDEs [28] gives:

$$u = axf_\eta(\eta),\ v = -\sqrt{av}f(\eta),\ \eta = y\sqrt{\frac{a}{\nu}},\ \theta(\eta) = \frac{T - T_\infty}{T_w - T_\infty}. \tag{10}$$

The radiation heat flux q_r is calculated as [30–33]:

$$qr = -\frac{4\sigma^*}{3k^*}\frac{\partial T^4}{\partial y}, \tag{11}$$

where k^* and σ^* are absorption Stephen–Boltzmann parameters; after using Rosseland's approach and by eliminating upper-order elements, we get T^4 as:

$$T^4 \cong 4T_\infty^3 T - 3T_\infty^4. \tag{12}$$

The radiation term is differentiated as follows:

$$\frac{\partial qr}{\partial y} = -\frac{16\sigma^* T_\infty^3}{3k^*}\frac{\partial^2 T}{\partial y^2}. \tag{13}$$

Combining Eqs. (13) and (8), we obtain:

$$u\frac{\partial T}{\partial x} + v\frac{\partial T}{\partial y} = \left(\frac{\kappa_{tnf}}{(\rho Cp)_{tnf}} + \frac{1}{(\rho Cp)_{tnf}}\frac{16\sigma^* T_\infty^3}{3k^*}\right)\frac{\partial^2 T}{\partial y^2} + \frac{Q_0(T - T_\infty)}{(\rho Cp)_{tnf}}. \tag{14}$$

By using similarity transformations, Eqs. (7) and (8) simplify to:

$$\Lambda\left(1 + \frac{1}{\Gamma}\right)\frac{d^3 f(\eta)}{d\eta^3} - A_2\left(\frac{df(\eta)}{d\eta}\right)^2 + A_2 f(\eta)\frac{d^2 f(\eta)}{d\eta^2} - \left(A_3 Q + A_1 Da^{-1}\right)\frac{df(\eta)}{d\eta} = 0, \tag{15}$$

$$\left(A_4 + Nr\right)\frac{d^2\theta(\eta)}{d\eta^2} + A_5\,\mathrm{Pr}\,\frac{d\theta(\eta)}{d\eta}f(\eta) + Ni\,\mathrm{Pr}\,\theta(\eta) = 0, \tag{16}$$

where.

$Ni = \frac{Q_0}{a(\rho C_p)_f}$ is the heat source/sink, $Q = \frac{\sigma_f H_0^2}{\rho_f a}$ is the magnetic parameter, $Da^{-1} = \frac{\nu_f}{K_1 a}$ is the inverse Darcy number, $\mathrm{Pr} = \left(\frac{\nu_f}{\alpha_f}\right)$ is the Prandtl number, $\Lambda = \frac{\mu_{eff}}{\mu_f}$ is the Brinkman/viscosity ratio parameter, $A_1 = \frac{\mu_{tnf}}{\mu_f}$, $A_2 = \frac{\rho_{tnf}}{\rho_f}$, $A_3 = \frac{\sigma_{tnf}}{\sigma_f}$, $A_4 = \frac{\kappa_{tnf}}{\kappa_f}$, $A_5 = \frac{(\rho C_p)_{tnf}}{(\rho C_p)_f}$.

The modified conditions of boundary are:

$$f = S,\ \frac{df}{d\eta} = d + b\frac{d^2 f}{d\eta^2},\ \frac{d\theta}{d\eta} = -Bi(1 - \theta),\ \text{as } \eta \to 0,\quad \frac{df}{d\eta} = 0,\ \theta = 0,\ \text{at } \eta \to \infty \tag{17}$$

Engineering quantities are calculated as

Nusselt number is studied as

$$Nu = \frac{xq_{\mathrm{w}}}{\kappa(T_{\mathrm{w}} - T_{\infty})},$$

where.

$q_{\mathrm{w}} = -\left(\left(\frac{16\sigma^* T_{\infty}^3}{3k*} + \kappa_{\mathrm{tnf}}\right)\right)\left(\frac{\partial T}{\partial y}\right)_{\mathrm{y}=0}$ is the heat flux at the wall.

Here,

$$Nu\mathrm{Re}^{-1/2} = -\left(A_4 + Nr\right)\frac{\mathrm{d}\theta(0)}{\mathrm{d}\eta}, \tag{18}$$

and skin friction studied as

$$C_{\mathrm{f}} = \frac{\tau_{\mathrm{w}}}{\rho_{\mathrm{f}}} = \left(1 + \frac{1}{\Gamma}\right)\frac{\mu_{\mathrm{eff}}}{\rho_{\mathrm{f}} U_{\mathrm{w}}^2}\left.\frac{\partial u}{\partial y}\right|_{\mathrm{y}=\mathrm{o}};$$

The above equation is formulated as

$$\mathrm{Re}^{1/2} C_{\mathrm{f}} = \Lambda\left(1 + \frac{1}{\Gamma}\right)\frac{\mathrm{d}^2 f(0)}{\mathrm{d}\eta^2}, \text{and} \tag{19}$$

Reynolds number is $\mathrm{Re} = \frac{U_{\mathrm{w}} x}{\nu_{\mathrm{f}}}$.

Analytical form of velocity equation

The analytic solution of Eq. (15) is with the B. Cs (17) are gained as follows [20]:

$$f(\eta) = S + d\frac{(1 - e^{-\delta\eta})}{\left(\delta + b\delta^2\right)}; \tag{20}$$

differentiating Eq. (20), we get:

$$\frac{\mathrm{d}f}{\mathrm{d}\eta} = \frac{de^{-\delta\eta}}{1 + b\delta}, \ \frac{\mathrm{d}^2 f}{\mathrm{d}\eta^2} = \frac{-d\delta e^{-\beta\eta}}{1 + b\delta}, \ \frac{\mathrm{d}^3 f}{\mathrm{d}\eta^3} = \frac{d\delta^2 e^{-\beta\eta}}{1 + b\delta}; \tag{21}$$

substituting Eqs. (20) and (21) in (15), we obtain

$$\begin{aligned}&\Lambda\left(1 + \frac{1}{\Gamma}\right)b\delta^3 + \left[\Lambda\left(1 + \frac{1}{\Gamma}\right) - A_2 Sb\right]\delta^2 \\ &-\left(A_3 Qb + A_1 Da^{-1} b - A_2 S\right)\delta \\ &-\left(A_3 Q + A_1 Da^{-1} + A_2 d\right) = 0,\end{aligned} \tag{22}$$

The above equation is rewritten as

$$\chi_1\delta^3 + \chi_2\delta^2 + \chi_3\delta + \chi_4 = 0, \tag{23}$$

where

$$\begin{aligned}&\chi_1 = \Lambda\left(1 + \tfrac{1}{\Gamma}\right)b, && \chi_2 = \left[\Lambda\left(1 + \tfrac{1}{\Gamma}\right) - A_2 Sb\right], \\ &\chi_3 = A_3 Qb + A_1 Da^{-1} b - A_2 S, && \chi_4 = \left(A_3 Q + A_1 Da^{-1} + A_2 d\right),\end{aligned}$$

and all possible roots of Eq. (23) can be written as

$$\begin{aligned}\delta_1 &= \frac{-\frac{\chi_2}{3\chi_1} - \left(2^{1/3}\left(-\chi_2^2 + 3\chi_1\chi_3\right)\right)}{3\chi_1\left(z + \sqrt{4\left(-\chi_2^2 + 3\chi_1\chi_3\right)^3 + (z)^2}\right)^{1/3}} \\ &+ \frac{1}{3\ 2^{1/3}\chi_1}\left(z + \sqrt{4\left(-\chi_2^2 + 3\chi_1\chi_3\right)^3 + (z)^2}\right)^{1/3}, \\ \delta_2 &= \frac{-\frac{\chi_2}{3\chi_1} + \left((1 + i\sqrt{3})\left(-\chi_2^2 + 3\chi_1\chi_3\right)\right)}{3\chi_1 2^{1/3}\left(z + \sqrt{4\left(-\chi_2^2 + 3\chi_1\chi_3\right)^3 + (z)^2}\right)^{1/3}} \\ &- \frac{(1 + i\sqrt{3})}{6\chi_1 2^{1/3}}\left(\begin{matrix} z \\ +\sqrt{4\left(-\chi_2^2 + 3\chi_1\chi_3\right)^3 + (z)^2}\end{matrix}\right)^{1/3}, \\ \delta_3 &= \frac{-\frac{\chi_2}{3\chi_1} + \left((1 + i\sqrt{3})\left(-\chi_2^2 + 3\chi_1\chi_3\right)\right)}{3\chi_1 2^{1/3}\left(z + \sqrt{4\left(-\chi_2^2 + 3\chi_1\chi_3\right)^3 + (z)^2}\right)^{1/3}} \\ &+ \frac{(1 + i\sqrt{3})}{6\chi_1 2^{1/3}}\left(\begin{matrix} z \\ +\sqrt{4\left(-\chi_2^2 + 3\chi_1\chi_3\right)^3 + (z)^2}\end{matrix}\right)^{1/3}\end{aligned} \tag{24}$$

where.

$z = \left(-2\chi_2^3 + 9\chi_1\chi_2\chi_3 - 27\chi_1^2\chi_4\right)$.

Analytical solution for the energy equation

To obtain an exact solution for Eq. (16), we consider a new term $q = \frac{\mathrm{Pr}}{\delta^2}e^{-\delta\eta}$, which is then solved by using the B. Cs in (17) are as follows:

$$q\frac{\mathrm{d}^2\theta}{\mathrm{d}q^2} + (1 - I + Jt)\frac{\mathrm{d}\theta}{\mathrm{d}q} + P\theta = 0, \tag{25}$$

where

$$I = \frac{A_5 Sb\,\mathrm{Pr}}{\left(A_4 + Nr\right)\delta} + \frac{A_5\,\mathrm{Pr}\,d}{\delta^2\left(A_4 + Nr\right)}, \ J = \frac{A_5\,\mathrm{Pr}\,d}{\left(A_4 + Nr\right)}, \ P = \frac{Ni\,\mathrm{Pr}}{\delta^2(A_4 + Nr)}.$$

The additional boundary conditions are as follows:

$$\frac{\mathrm{Pr}}{\delta}\frac{\mathrm{d}\theta}{\mathrm{d}q}\left(\frac{\mathrm{Pr}}{\delta^2}\right) = Bi\left(1 - \theta\left(\frac{\mathrm{Pr}}{\delta^2}\right)\right), \text{ and } \theta(0) = 0; \tag{26}$$

to calculate Eq. (25) by using a power series method, $\theta(q) = \sum_{r=0}^{\infty} a_r q^{r+k}$; applying Frobenius method to the problem, the exact solution is obtained as:

$$\theta(q) = \frac{\frac{Bi}{A_4}\left(e^{(-\delta\eta)}\right)_1^{\frac{k_1+k_2}{2}} M_1\left[\frac{k_1+k_2}{2}, k_2+1, -Jpe^{(-\delta\eta)}\right]}{\left(\delta\frac{k_1+k_2}{2}\right)_1 M_1\left[\frac{k_1+k_2}{2}, k_2+1, -Jp\right] - \frac{Jp}{k_2+1}{}_1 M_1\left[\frac{k_1+k_2}{2}+1, k_2+2, -Jp\right]} + \frac{P}{A_4}{}_1 M_1\left[\frac{k_1+k_2}{2}, k_2+1, -Jp\right], \tag{27}$$

where

$$P = \frac{\Pr Ni}{\delta^2(A_4+Nr)},\ k_1 = I,\ k_2 = \sqrt{I^2-4P},\ p = \frac{\Pr}{\delta^2},$$
$$I = \frac{A_5 Sb\Pr}{(A_4+Nr)\delta} + \frac{A_5\Pr d}{\delta^2(A_4+Nr)},\ J = \frac{A_5\Pr d}{(A_4+Nr)}, \tag{28}$$

Thermophysical properties of nanoparticle

Density in ternary nanofluid:

$$\frac{\rho_{tnf}}{\rho_f} = (1-\phi_{Ag})\left\{(1-\phi_{Cu})\left[(1-\phi_{TiO_2}) + \phi_{TiO_2}\frac{\rho_{TiO_2}}{\rho_f}\right] + \phi_{Cu}\frac{\rho_{Cu}}{\rho_f}\right\} + \phi_{Ag}\frac{\rho_{Ag}}{\rho_f}. \tag{29}$$

Dynamic viscosity [34, 35] is defined as:

$$\mu_{tnf} = \frac{\mu_f}{(1-\phi_{Ag})^{2.5}(1-\phi_{Cu})^{2.5}(1-\phi_{TiO_2})^{2.5}}. \tag{30}$$

Thermal conductivities in ternary nanofluid [34]:

$$\frac{\kappa_{tnf}}{\kappa_{hnf}} = \frac{\kappa_{Ag}+2\kappa_{hnf}-2\phi_{Ag}(\kappa_{hnf}-\kappa_{Ag})}{\kappa_{Ag}+2\kappa_{hnf}+\phi_{Ag}(\kappa_{hnf}-\kappa_{Ag})},$$
$$\frac{\kappa_{hnf}}{\kappa_{nf}} = \frac{\kappa_{Cu}+2\kappa_{nf}-2\phi_{Cu}(\kappa_{nf}-\kappa_{Cu})}{\kappa_{Cu}+2\kappa_{nf}+\phi_{Cu}(\kappa_{nf}-\kappa_{Cu})}, \tag{31}$$
$$\frac{\kappa_{nf}}{\kappa_f} = \frac{\kappa_{TiO_2}+2\kappa_f-2\phi_{TiO_2}(\kappa_f-\kappa_{TiO_2})}{\kappa_{TiO_2}+2\kappa_f+\phi_{TiO_2}(\kappa_f-\kappa_{TiO_2})}.$$

The electrical conductivities are given by

$$\frac{\sigma_{tnf}}{\sigma_{hnf}} = 1 + \frac{3\left(\frac{\sigma_{Ag}}{\sigma_{hnf}}-1\right)\phi_{Ag}}{\left(\frac{\sigma_{Ag}}{\sigma_{hnf}}+2\right) - \left(\frac{\sigma_{Ag}}{\sigma_{hnf}}-1\right)\phi_{Ag}},$$
$$\frac{\sigma_{nf}}{\sigma_f} = 1 + \frac{3\left(\frac{\sigma_{TiO_2}}{\sigma_f}-1\right)\phi_{TiO_2}}{\left(\frac{\sigma_{TiO_2}}{\sigma_f}+2\right) - \left(\frac{\sigma_{TiO_2}}{\sigma_f}-1\right)\phi_{TiO_2}}, \tag{32}$$
$$\frac{\sigma_{hnf}}{\sigma_{nf}} = 1 + \frac{3\left(\frac{\sigma_{Cu}}{\sigma_{nf}}-1\right)\phi_{Cu}}{\left(\frac{\sigma_{Cu}}{\sigma_{nf}}+2\right) - \left(\frac{\sigma_{Cu}}{\sigma_{nf}}-1\right)\phi_{Cu}}.$$

Kalidasan [33] specified the thermal capacity of ternary nanofluid quantity as follows:

$$\frac{(\rho C_p)_{tnf}}{(\rho C_p)_f} = (1-\phi_{Ag})\left\{(1-\phi_{Cu})\left[(1-\phi_{TiO_2}) + \phi_{TiO_2}\frac{(\rho C_p)_{TiO_2}}{(\rho C_p)_f}\right] + \phi_{Cu}\frac{(\rho C_p)_{Cu}}{(\rho C_p)_f}\right\} + \phi_{Ag}\frac{(\rho C_p)_{Ag}}{(\rho C_p)_f}. \tag{33}$$

Results and discussion

The current analysis focused on the impact of Brinkman and MHD across a Bingham fluid movement with energy distribution and also explored the influence of solar radiation with velocity slip. The PDE equations are solved using similarity transformations and converted to ODEs and further studied the plots of upper and lower solutions response on the ternary nanofluid as follows: For our study, setting the numerical choice of the Prandtl number Pr is 6.7 for sodium alginate, and the range of terms is taken as $-5 \le d \le 5$, $-5 \le S \le 5$, $0.1 \le Q \le 4$, $1 \le Bi \le 3$, $0.5 \le Da^{-1} \le 4$, $-0.5 \le Ni \le 0.5$, $0.1 \le Nr \le 2$, and $0.01 \le \phi < 0.03$, and thermophysical characteristics are given in Table 1. After these limiting values, the graphs cannot be plotted, and

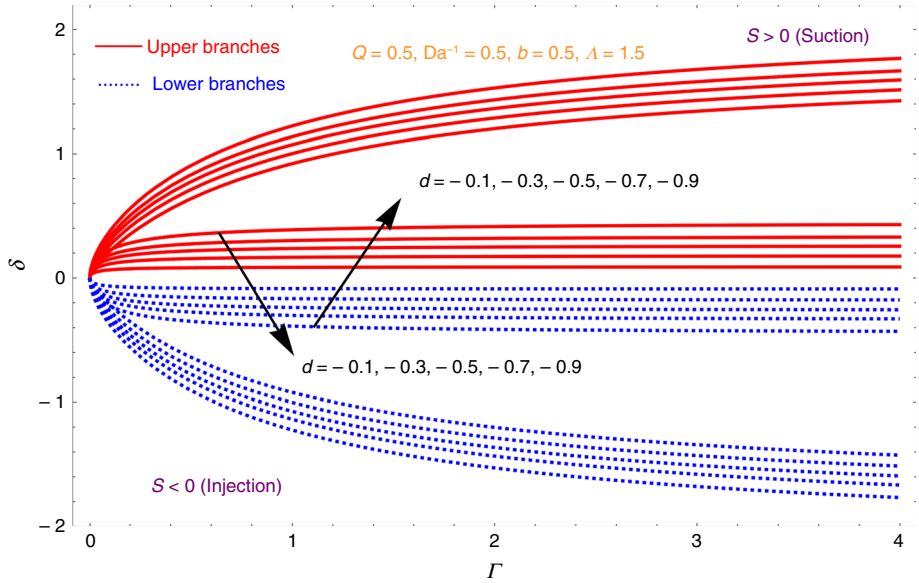

Fig. 2 Solution graph for stretching/shrinking parameter

several physical parameters are explained through graphs in the below section.

Figure 2 represents the solution δ versus Bingham parameter graph for variations of stretching/shrinking parameter. The higher branches are portrayed by solid red lines, whereas the other branch solutions are given by dashed blue lines, and the graph is taken for both suction and injection conditions, decreasing the d parameter for suction case; boundary layer thickness increases and shows reverse phenomena for injection case.

Figure 3 portrays the solution graph of d concerning a magnetic field; the higher branches are displayed by solid red lines, whereas the other branch solutions are denoted by dashed blue lines, keeping all physical parameters constant and the graph taken for mass injection case; increasing the parameter d, we see that upper branches increase dramatically and lower branches show decreasing nature.

Figure 4 represents the solution graph of d concerning mass transpiration; the higher branches are displayed by solid red lines, whereas the other branch solutions are denoted by dashed blue lines, keeping all physical parameters constant; increasing the values of d generates rising in the solution in the upper branches, and for the same solution, values of lower branch decrease dramatically.

Figure 5 represents the solution graph of the Bingham parameter with respect to the Brinkman parameter; the higher branches are shown by solid red lines; a graph taken for both suction and injection, in both cases for

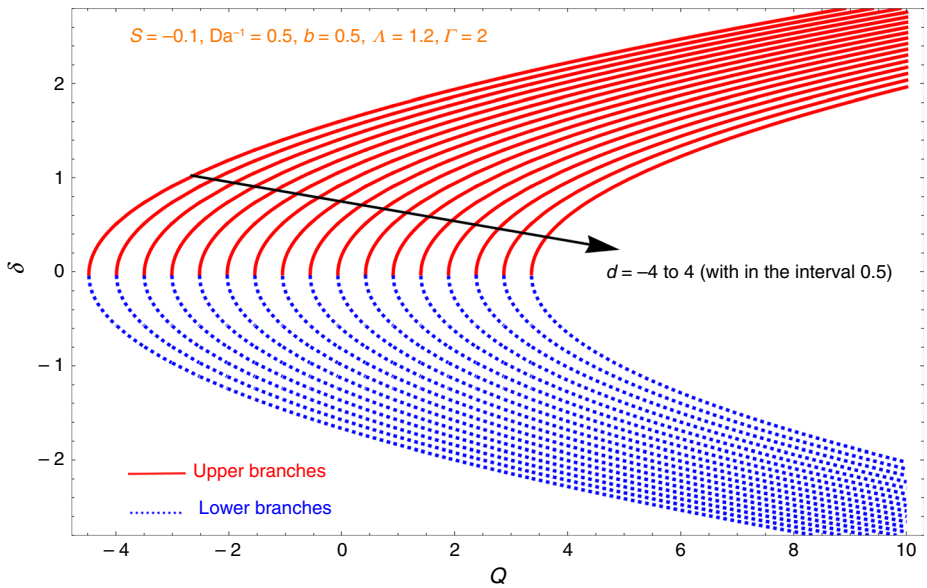

Fig. 3 Solution graph for stretching/shrinking parameter Q

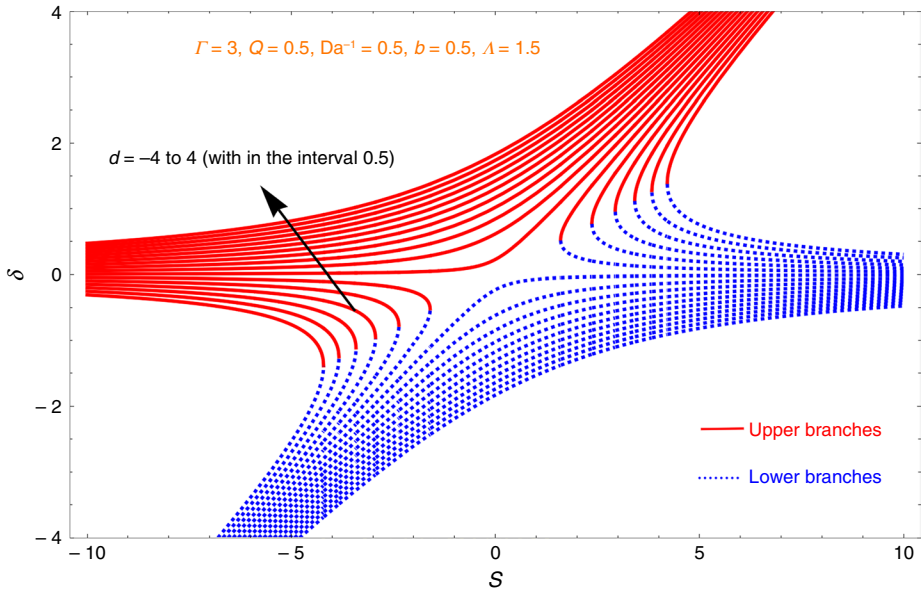

Fig. 4 Solution graph for stretching/shrinking parameter versus S

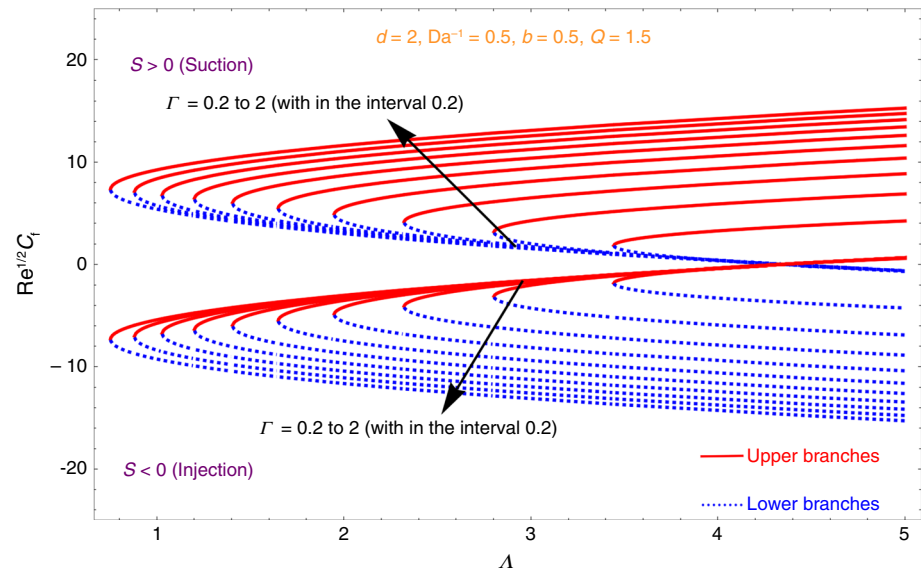

Fig. 5 Skin friction graph for Bingham parameter versus Λ

the enhancing value of λ, upsurges the solution boundary layer thickness, and for injection case shows reverse phenomena; skin friction coefficient is a calculator of the frictional resistance to fluid flow along a surface. The Bingham parameter is a rheological parameter that characterizes the movement of Bingham plastic fluids, which are materials that produce a yield stress and shear rate and shear stress above the yield stress relationship; the skin friction decreases with enhancing volume fraction values of the Bingham parameter. In both, the increasing value of λ upsurges the solution boundary layer thickness and for injection case shows reverse phenomena.

Figure 6 portrays the Nusselt number graph for different choices of d versus, keeping all physical parameters constant. Nusselt number decays with increasing stretching parameters and rises with increasing shrinking parameters. The graph is taken for the heat sink case; here, increase in the d parameter upsurges the solution boundary layer in both upper and lower branches. Figure 7 portrays the skin friction plot for various choices of the Bingham parameter versus d, impressing the values of the Bingham term enhancing the skin friction, and both branch solutions show increasing nature.

Figure 8 portrays the solution graph of the stretching parameter with respect to the Bingham parameter; higher

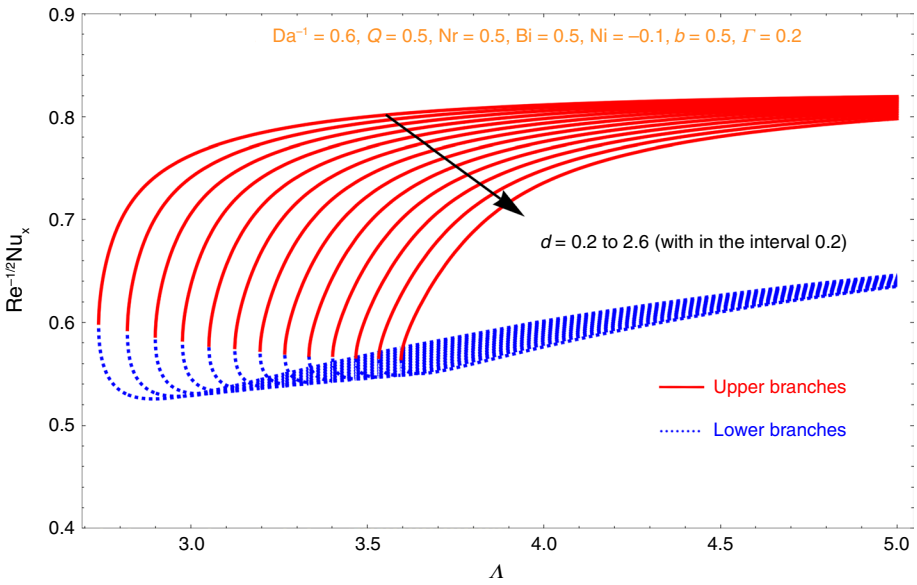

Fig. 6 Nusselt number graph for various choices of d versus Λ

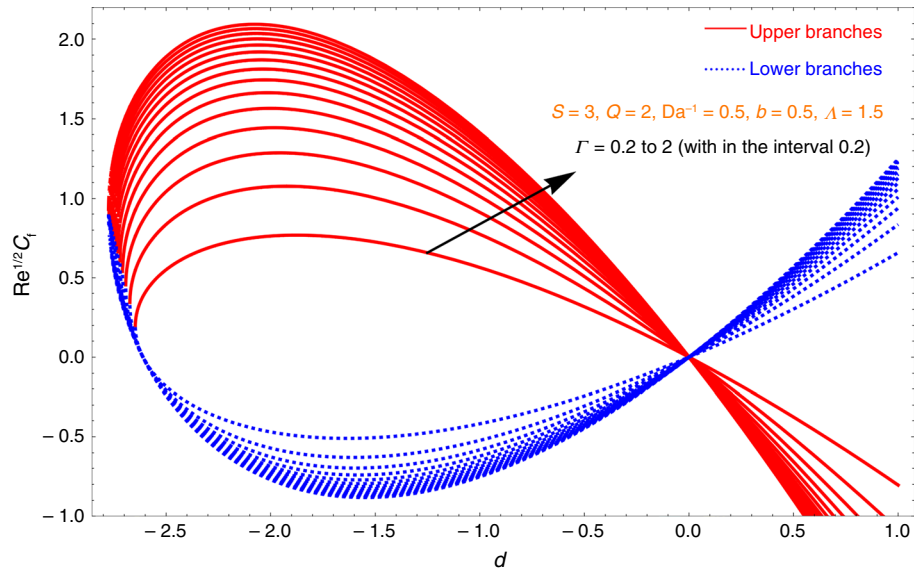

Fig. 7 Skin friction graph for various choices of Bingham term versus d

branch solutions are displayed by red solid lines, while lower branch solutions are shown by blue dashed lines; in the graph taken for both S values, for the suction case, both upper and lower branches are in the positive region, and for injection case, both branches are in the negative region, enhancing the stretching parameter which rises the skin friction as well as boundary layer thickness.

Figure 9a and b portrays the plots for the momentum profile for the different choices of the Γ parameter for both boundaries; the geometry of the movement and the Bingham number determine the momentum profile of a Bingham fluid. It represents the yield stress to viscous stress ratio; 9a represents the plot for stretching boundary enhancing that the Bingham values decays the momentum, and 9b represents the plot for shrinking boundary which exhibits the upper and lower branches, while increasing the Bingham parameter upper branch shows enhancing nature and lower branch shows decaying nature for same parametric values.

Figure 10a and b denotes the graphs of momentum profile for the different choices of Da^{-1} for both expanding and shrinking surfaces; the momentum profile of Da^{-1}, the fluid movement rate through a permeable media, is studied by Darcy's law that gives the movement rate is proportional to the pressure gradient; 10a represents the plot for stretching boundary, upsurging that the Da^{-1} values decay the velocity of the fluid, and 10b represents the plot for the shrinking boundary which exhibits the upper and lower branches, while increasing the Da^{-1}, both branches show decaying nature; in both expanding and shrinking boundaries, upsurging the Da^{-1} decreases the velocity of flow.

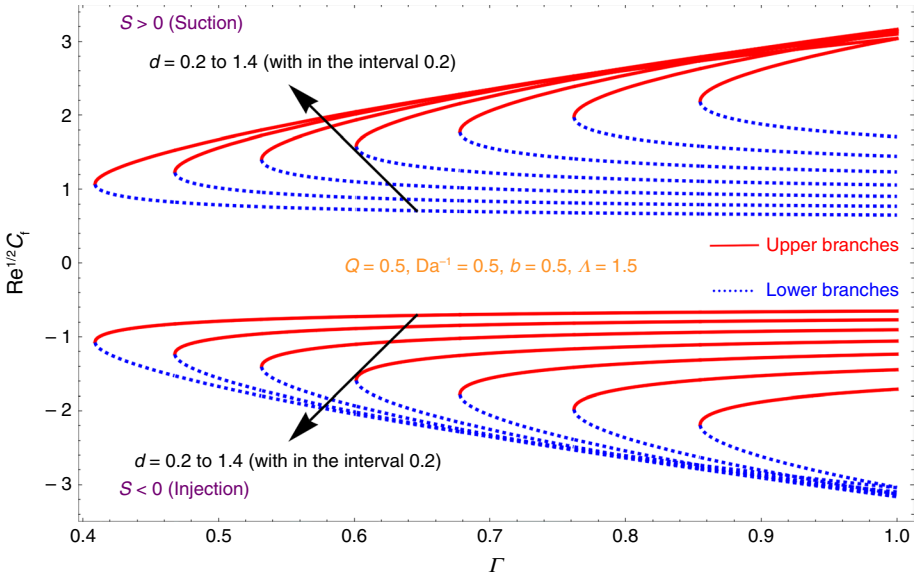

Fig. 8 Skin friction graph for stretching parameter versus Bingham parameter

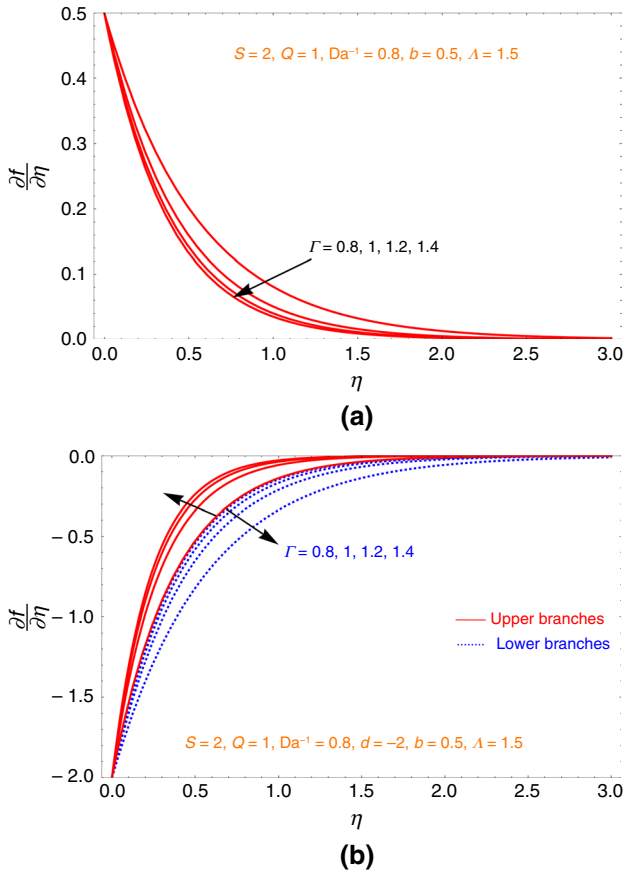

Fig. 9 **a** Velocity plot for Bingham parameter versus similarity variable, **b** Velocity plot for Bingham parameter for shrinking boundary

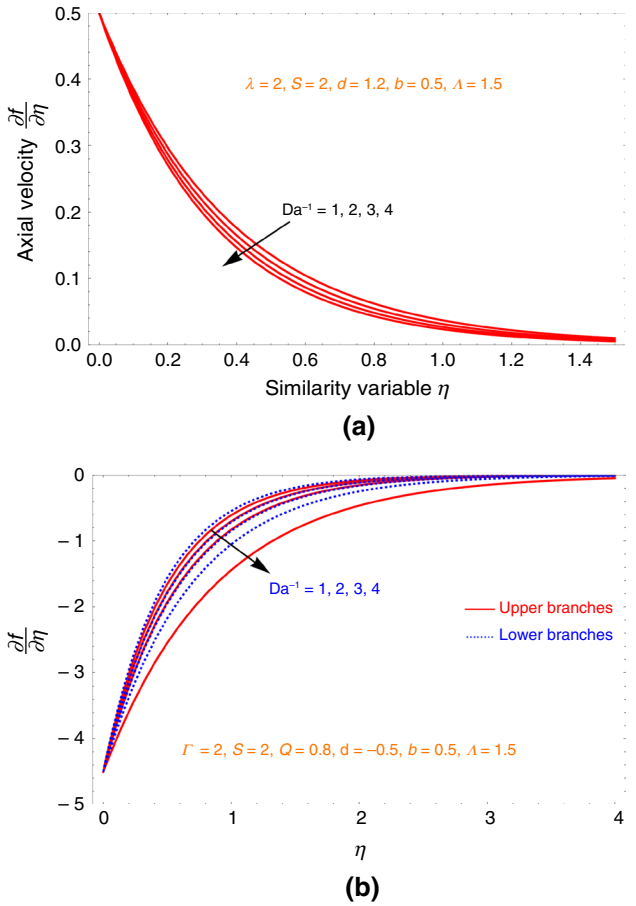

Fig. 10 **a** Velocity graph for Da^{-1}, **b** Velocity plots for inverse Darcy number for shrinking surface

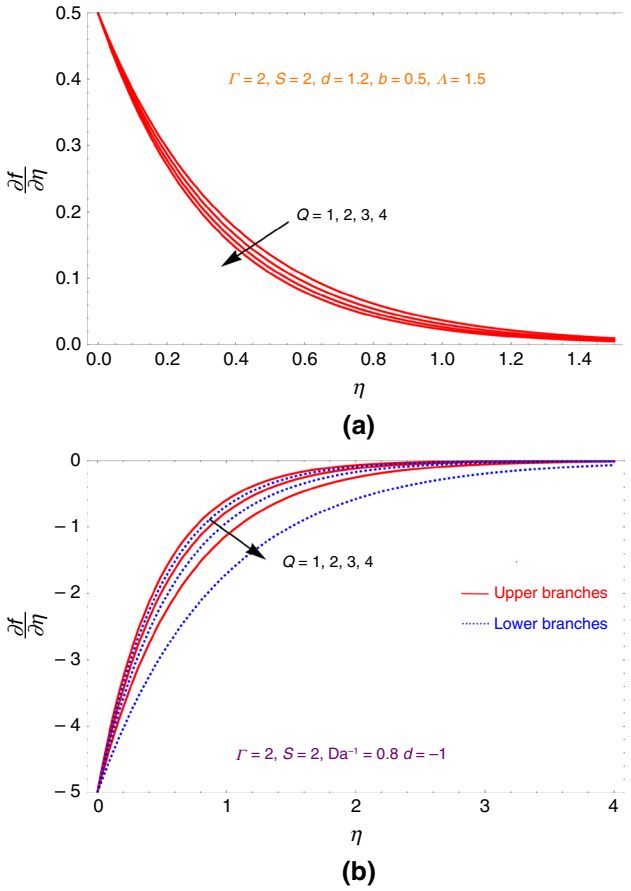

Fig. 11 **a** Velocity plot for magnetic field, **b** Velocity plot for magnetic field for shrinking boundary

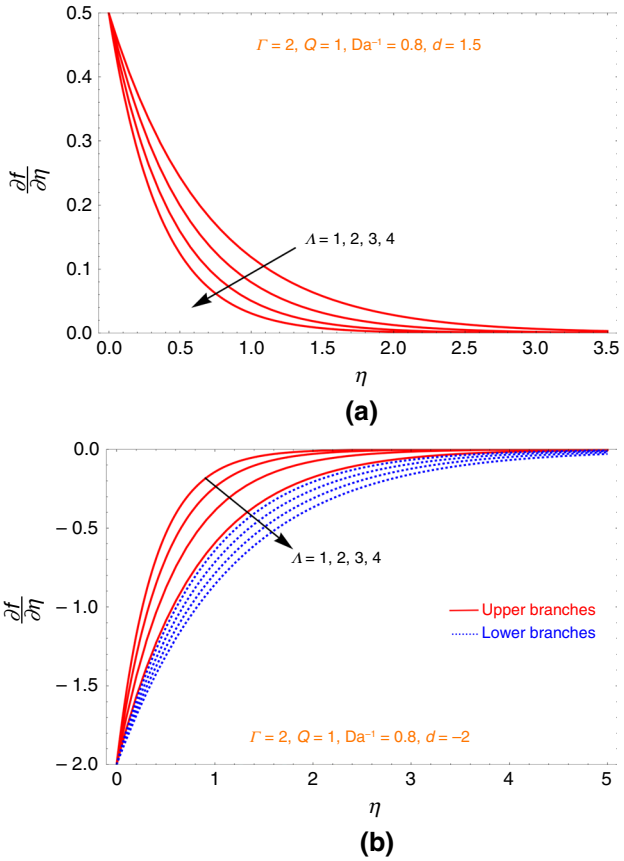

Fig. 12 **a** Velocity graph for Brinkman ratio, **b** Velocity graph for Brinkman ratio for shrinking surface

Figure 11a and b portrays the plots of the momentum profile for the various choices of Q for both expanding and shrinking surfaces and the velocity profile of Q. A Lorentz force is exhibited by the magnetic field, which opposes the motion of the fluid; this force is dissipative and can be used to suppress velocity fluctuations; the Lorentz force acts on the fluid due to the collision in the magnetic field and the electrical conductivity of the liquid; 11a represents the plot for stretching surface enhancing that the Q values decays the velocity, and 11b represents the plot for the shrinking boundary which exhibits the upper and lower branches; while increasing the Q parameter, both higher and lower branches show decaying nature, and in both expanding and shrinking surfaces, upsurging the Q decays the momentum of the fluid movement.

Figure 12a and b portrays the plots of the momentum regime for the different choices of the Brinkman term for both expanding and shrinking surfaces. The Brinkman number (Br) is a non-dimensional number that is commonly used in polymer extracting to describe heat conduction from a wall to a moving viscous liquid, the impact of the Brinkman number on the momentum of a fluid is that it is associated with reduced velocity distribution and increased skin friction; 12a represents the plot for stretching boundary enhancing that the Br values decays the velocity, and 12b represents the plot for the shrinking boundary which exhibits the upper and lower branches; while increasing the Brinkman number, both branches show decreasing nature, and in both boundaries, enhancing the Brinkman number reduces the momentum of the fluid.

Figure 13a and b portrays the plots of the velocity for the various choices of velocity slip parameter for both boundaries; as the velocity slip rises, the flow resistance decreases, leading to a decays in the skin friction and an upsurge in the Nusselt number; 13a portrays the plot for stretching boundary enhancing the velocity slip values decay the velocity, and 13b represents the plot for shrinking boundary which exhibits the upper and lower branches; while increasing the velocity slip, both branches show decreasing nature, and in both expanding and shrinking boundaries, enhancing the velocity slip number decays the momentum.

Figure 14a and b portrays the plots of the energy regime for the different choices of Ni parameter for both expanding and shrinking boundaries, and the impact of heat source on the temperature of a liquid depends on the type of fluid

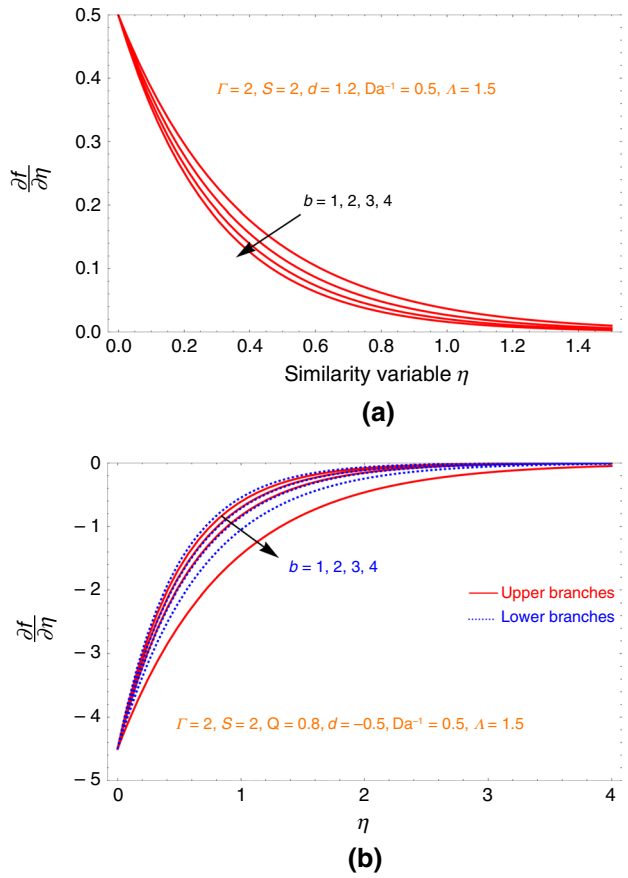

Fig. 13 **a** Slip parameter effect on velocity profile, **b** Velocity slip parameter graph for velocity profile

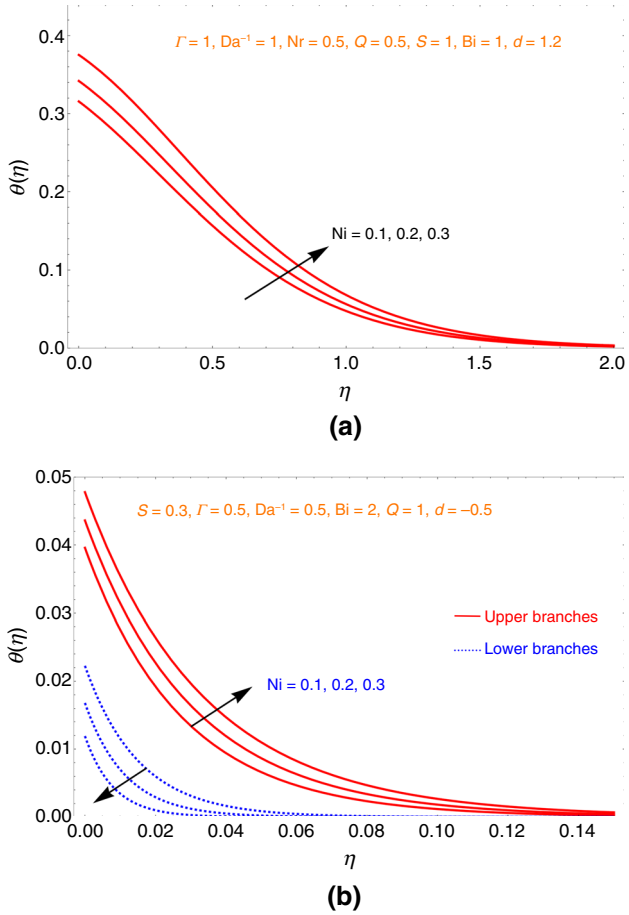

Fig. 14 **a** Temperature graph for *Ni* parameter, **b** Temperature graph for *Ni* parameter for shrinking boundary

movement and the physical parameters involved, and a heat source rises the heat of the liquid, which tends to rise in the fluid temperature, while a heat sink decreases the thermal conductivity, which tends to a reduce in the fluid temperature; 14a represents the plot for stretching boundary increasing the *Ni* values increases the temperature, 14b portrays the plot for shrinking boundary which exhibits the upper and lower branches, while increasing the *Ni* upper shows increasing nature, and lower branch shows decaying nature; in both expanding and shrinking surfaces, enhancing the *Ni* number raises upsurges the temperature of the liquid movement.

Figure 15a and b represents the plots of the temperature for the different choices of Bi parameter for both expanding and shrinking sheets, the Biot number (Bi) is a non-dimensional quantity utilized in heat transfer, and it can affect the temperature distribution in various heat transfer problem; when the Biot number is greater than about 0.1, heat conduction inside the body offers more significant thermal resistance, and temperature gradients are more pronounced; 15a represents the plot for stretching boundary; increasing the Bi values increases the temperature. 15b portrays the plot for a shrinking boundary which exhibits the upper and lower branches, while increasing the Bi both branches show upsurging; in both expanding and shrinking surfaces, raising the Bi number enhances the temperature of the liquid movement.

Figure 16a and b portrays the plots of the energy profile for the different values of the velocity slip term for both expanding/shrinking boundaries, and velocity slip comes when the fluid momentum at the boundary of the wall varies from the velocity of the wall itself; 16a represents the plot for stretching boundary upsurging the momentum slip choices which enhance the temperature, and 16b portrays the plot for the shrinking boundary which exhibits the upper and lower branches, while increasing the velocity slip, both upper and lower branches show enhancing, and in both expanding and shrinking surfaces, enhancing the momentum slip number enhances the energy of the movement of the liquid.

Figure 17a and b portrays the plots of the temperature for the different numbers of magnetic field parameters for both expanding and shrinking surfaces, and magnetic field term directly impacts the energy. Physically, a rise in the MHD

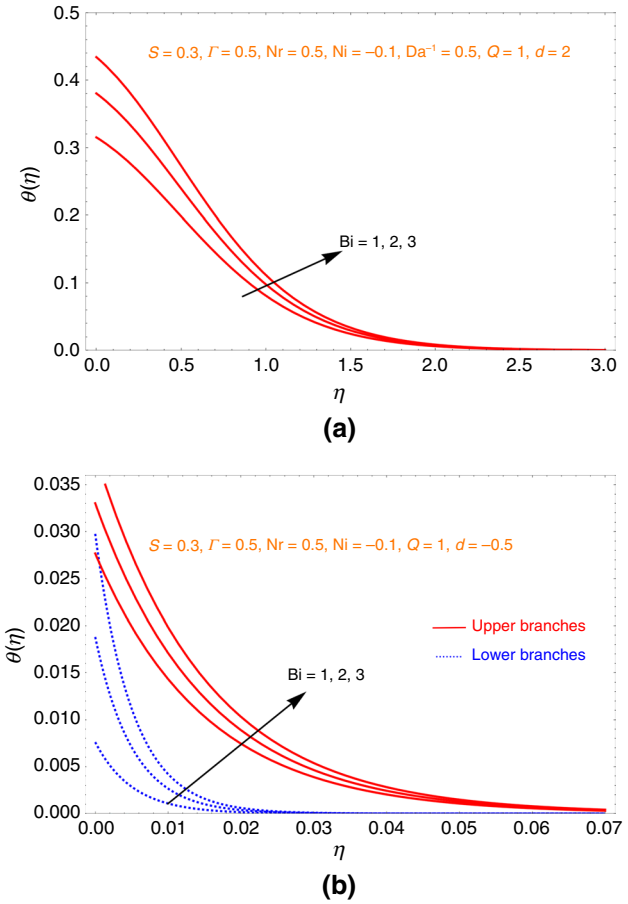

Fig. 15 **a** Bi parameter effect on temperature, **b** Temperature graph for Bi parameter for shrinking surface

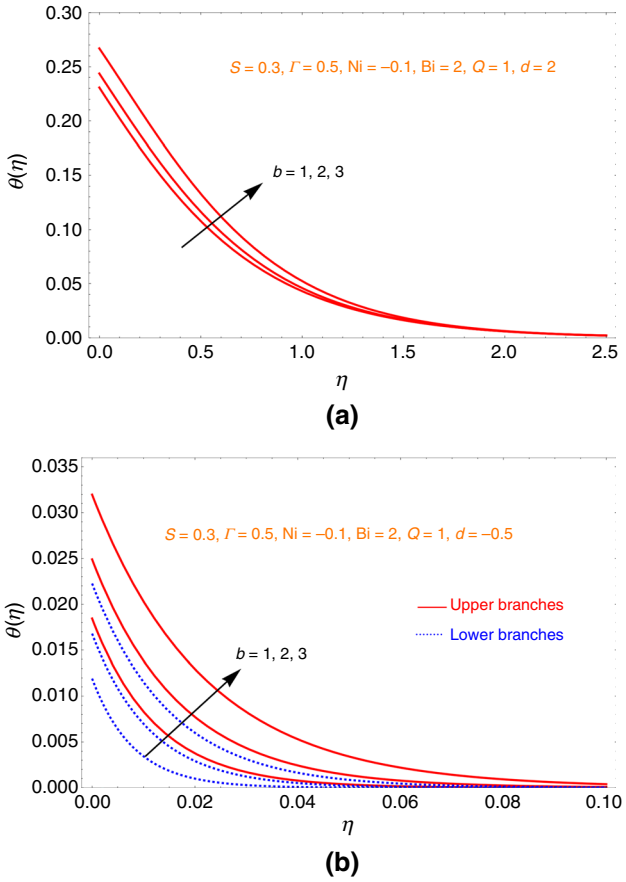

Fig. 16 **a** Temperature plots for velocity slip parameter, **b** Temperature graph for velocity slip parameter for shrinking surface

provides difficulties for the liquid to move, which tends to enhance in the thermal rate; 17a portrays the plot for expanding boundary upsurging the magnetic field values decays the temperature. 17b represents the plot for shrinking boundary which exhibits the upper and lower branches, while increasing the magnetic field, both upper and lower branches show increase, and in stretching increase, the magnetic field number shows decaying nature but in shrinking surface, increasing magnetic field number shows reverse phenomena.

Figure 18a and b portrays the plots for the temperature regime for the different numbers of the Γ parameter for both expanding and shrinking boundaries; Γ is a term used to demonstrate the rheological behavior of a fluid, particularly non-Newtonian fluids. Bingham liquid is a shear-thinning fluid that exhibits a viscosity at zero shear rates and yield stress below gains no flow; 18a represents the plot for stretching boundary enhancing the Bingham parameter values reduce the temperature, and 18b portrays the plot for the shrinking boundary which exhibits the upper and lower branches, while enhancing the Bingham parameter upper shows increasing nature, but lower branch shows decaying nature.

Figure 19a and b displays the graphs of *Nr* for the temperature, thermal radiation plays a major role in monitoring thermal transfer in polymer industries, thermal radiation is the emission of energy from a surface due to its temperature, and it can affect the temperature of the fluid it interacts with; 19a portrays the plot for stretching boundary increasing the *Nr* values increases the temperature, and 19b represents the plot for the shrinking boundary which exhibits the upper and lower branches, while increasing the *Nr,* both higher and lower branches show upsurging nature; in both expanding and shrinking surfaces, increasing the *Nr* number shows increasing the thermal boundary layer.

Figure 20a and b portrays the plots for the temperature for the different choices of the Brinkman term for both expanding and shrinking boundaries, and the Brinkman number can affect the temperature, as it denotes the ratio of viscous heat production to molecular conduction when the Brinkman term is higher; the conduction of heat generated by viscous dissipation is slower; 20a represents the plot for stretching boundary increasing the Brinkman values upsurges the

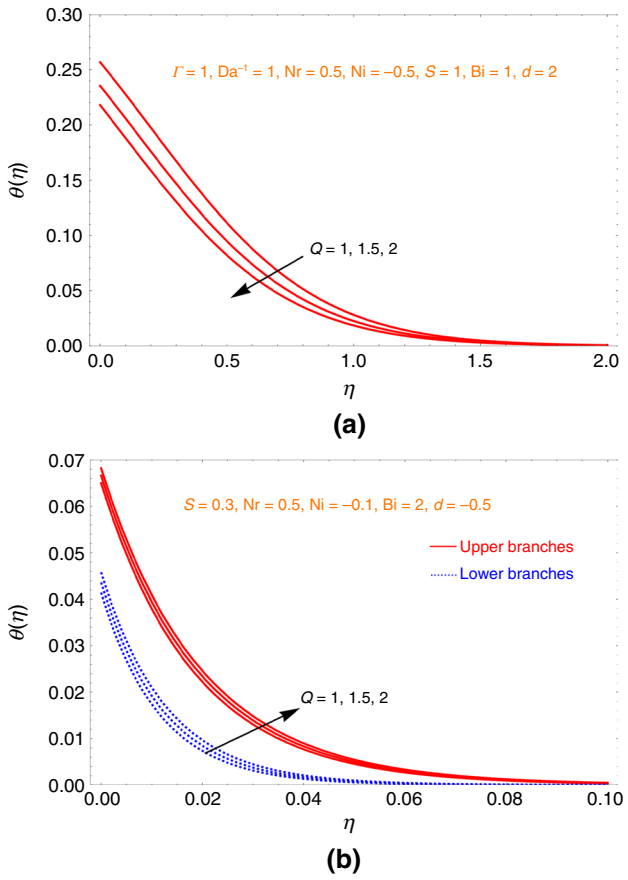

Fig. 17 **a** Temperature plot for magnetic field parameter (Q), **b** Energy graph for magnetic field on shrinking boundary

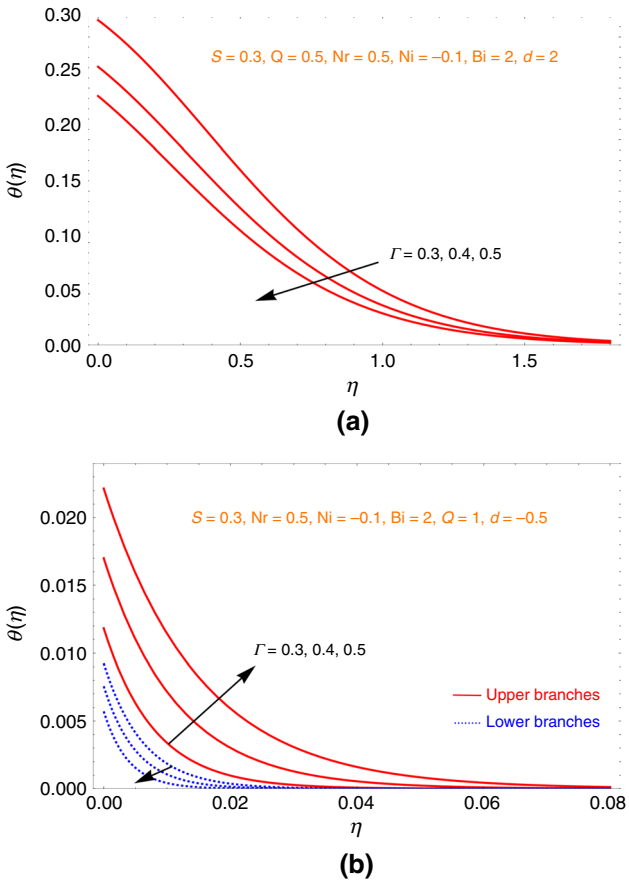

Fig. 18 **a** Temperature graph for Bingham term, **b** Temperature graph for Bingham parameter for the shrinking surface

temperature, and 20b portrays the plot for the shrinking boundary which exhibits both branches, while increasing the Brinkman, both branches show upsurging nature, and in both expanding and shrinking surfaces, increasing the Brinkman number shows increasing the thermal boundary layer.

Figure 21a–d represents the streamlined graphs for different choices of magnetic field, mass transpiration, Bingham parameter, and Brinkman number. Streamlines play a crucial role in visualizing the flow behavior in fluid dynamics, as they represent the trajectories followed by fluid particles, thereby offering clear insight into the structure and direction of the flow field. In the context of streamlined graphs for various values of magnetic field, mass transpiration, Bingham term, and Brinkman number, streamlines help reveal how each parameter influences the velocity distribution, flow separation, and boundary layer development. For instance, variations in the magnetic field can alter the Lorentz force, affecting flow retardation, while mass transpiration modifies the boundary layer thickness by either injecting or suction of fluid. The Bingham parameter reflects the non-Newtonian nature of the fluid, influencing yield stress behavior and flow resistance, and the Brinkman number indicates viscous dissipation effects within porous media. Through streamline patterns, one can visually assess how these parameters collectively shape the flow characteristics, making them an essential diagnostic tool for interpreting complex fluid behavior in magnetohydrodynamic and non-Newtonian systems.

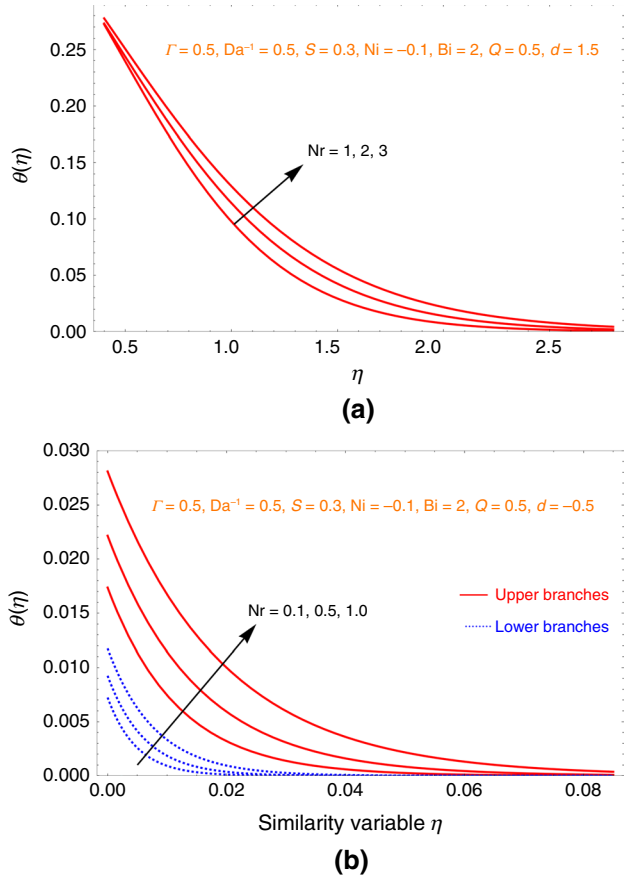

Fig. 19 **a** Thermal radiation effect on temperature profile, **b** Energy profile graph for radiation parameter for a shrinking surface

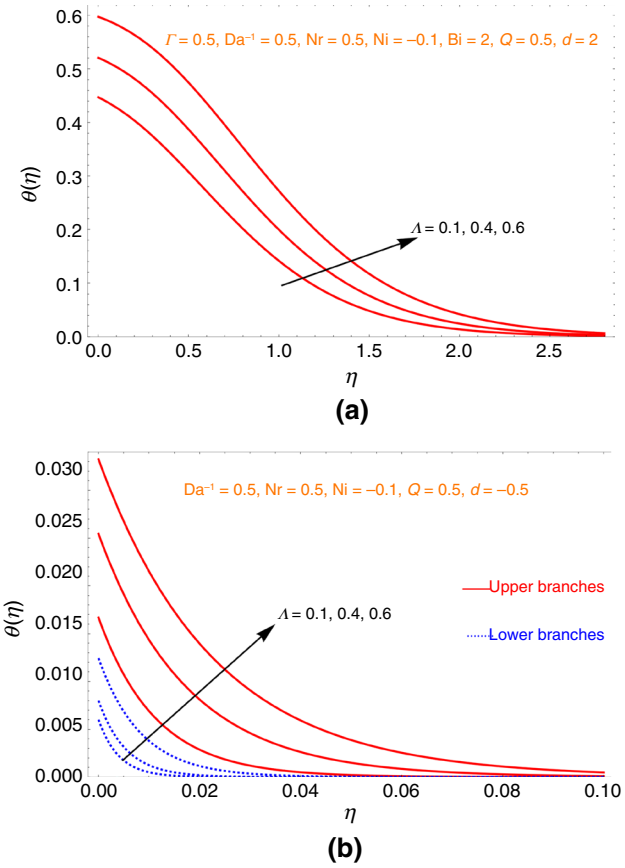

Fig. 20 **a** Temperature graph for Brinkman parameter, **b** Temperature graph for Brinkman parameter for the shrinking surface

Concluding remarks

The present work investigated the impact of magnetic field applied to a ternary nanofluid flow; the authors observed that there is a dearth of research on Bingham ternary nanofluids with the circumstance of velocity slip and temperature jump boundary conditions and impact of MHD and thermal radiation on ternary nanofluids and utilized the research gap. Also, the authors studied the Darcy–Brinkman's effect on the flow. The governing equations are formulated to ODEs by using suitable variables and then calculated by an analytical approach. The following conclusions can be made:

- Increasing the magnetic field decays the momentum of the fluid and enhances the thermal boundary layer.
- Increasing inverse Darcy number decreases the momentum of the fluid and raises the thermal boundary layer.
- Increasing the Bingham parameter decays the velocity of the fluid and raises the thermal boundary layer.
- Enhancing the slip values decays the momentum of the fluid.

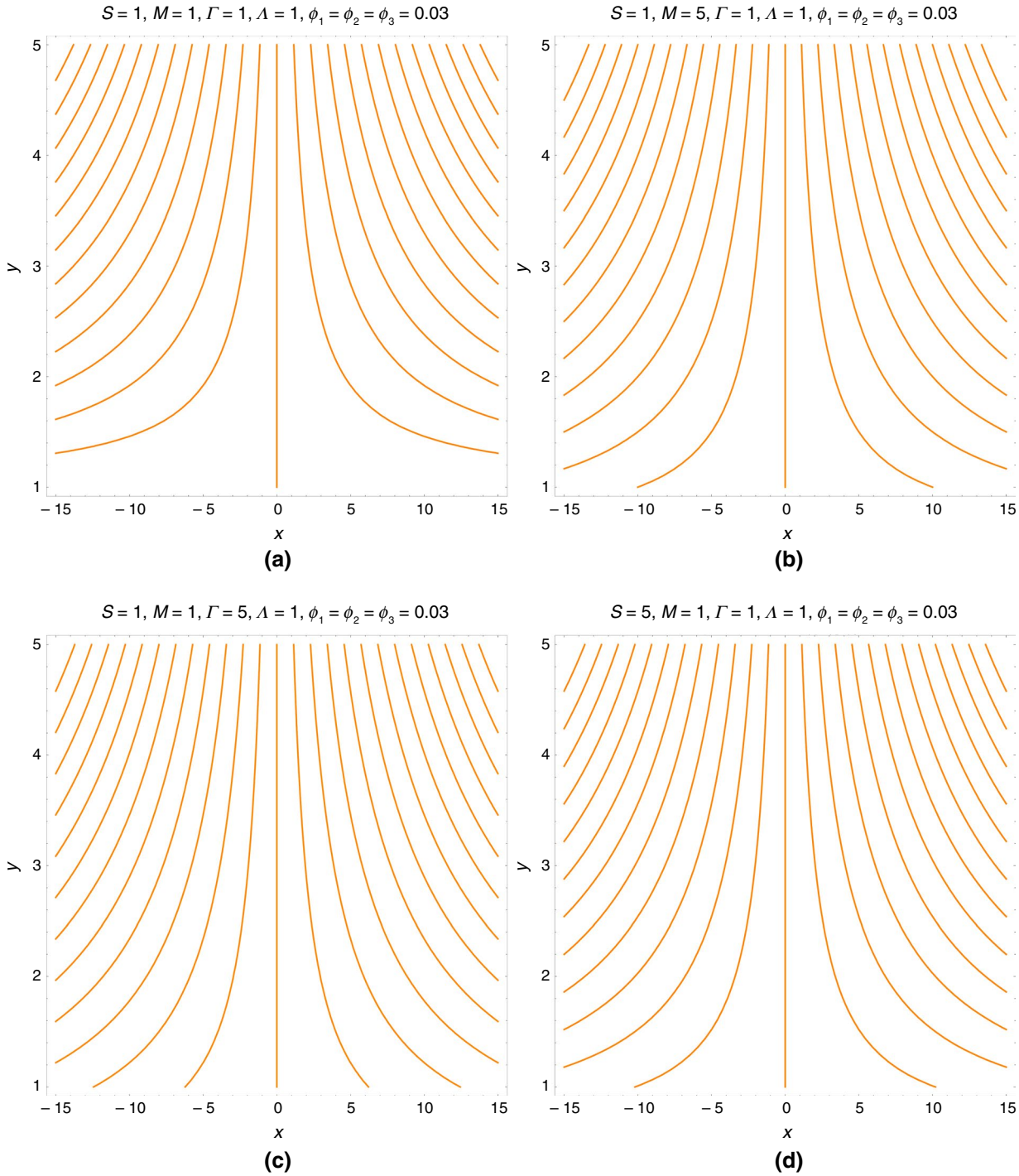

Fig. 21 **a**–**d** represent the streamlined graphs for different choices of magnetic field, mass transpiration, Bingham parameter, and Brinkman number

- Enhancing the thermal radiation and volume fractions upsurges the thermal boundary layer.
- Enhancing the Brinkman parameter decreases the momentum profile and raises the thermal boundary layer.

Limitations of the current study compared to previous research are:

- $\lim_{\substack{\phi, Q_o \to 0 \\ \Lambda \to 0 \\ Da^{-1} \to 0}} \{\text{present results}\} \to \{\text{results of Hamid et al. [26]}\}$

- In the absence of porous medium and inclined angle and adding of hybrid nanofluid, {present results} →{results of Khan et al. [28]}.

The present work can be extended by using several physical fluid models effects such as Maxwell fluid, couple stress fluid, and Williamson fluids over various boundaries such as convergent/divergent channel, exponential stretching sheet, wedge, among others.

Limitations and future study of the current analysis

Despite the promising findings, the study has certain limitations, particularly the assumption of idealized boundary conditions and the lack of experimental validation to support the theoretical results. The influence of dynamic environmental factors and complex geometries was not explored, which may limit practical applicability. However, the research opens new avenues for future work, especially in incorporating real-world boundary effects like surface roughness, transient behavior, and extending the analysis to three-dimensional flows. There is also significant scope for integrating advanced computational techniques and experimental studies to validate and enhance the predictive accuracy of Bingham ternary nanofluid models in practical thermal systems.

Acknowledgement L. M. P. and D. L. gratefully acknowledge financial support from the Centers of Excellence with BASAL/ANID CIA250002, CEDENNA. U. S. M. sincerely thanks Prof. D. L. Instituto de Alta Investigación, Universidad de Tarapacá, Casilla 7 D, Arica 1000000, Chile, for the kind hospitality, as well as the University of Tarapacá for the Visiting Professorship-2024, support.

Author contributions Conceptualization was done by S.M.S and U.S.M; methodology was done by S.M.S, L.M.P, and D.L; data collection was done by U.S.M, S.M.S, and D.L; data analysis was done by S.M.S, D.L, and U.S.M; writing—original draft was done by S.M.S and U.S.M; writing—review and editing was done by S.M.S and U.S.M; supervision was done by D.L and L.M.P; funding acquisition was done by D.L and L.M.P; resources were done by D.L and L.M.P; visualization was done by S.M.S and U.S.M.

Declarations

Conflict of interest The authors have no conflict of interest to declare.

References

1. Ramzan M, Ali F, Akkurt N, Saeed A, Kumam P, Galal AM. Computational assessment of Carreau ternary hybrid nanofluid influenced by MHD flow for entropy generation. J Magn Magn Mater. 2023;567: 170353. https://doi.org/10.1016/j.jmmm.2023.170353.
2. Alharbi KAM, et al. Computational valuation of Darcy ternary-hybrid nanofluid flow across an extending cylinder with induction effects. Micromachines. 2022;13(4): 4. https://doi.org/10.3390/mi13040588.
3. Sahoo RR, Kumar V. Development of a new correlation to determine the viscosity of ternary hybrid nanofluid. Int Commun Heat Mass Transf. 2020;111: 104451. https://doi.org/10.1016/j.icheatmasstransfer.2019.104451.
4. Sachhin SM, Mahabaleshwar US, Swaminathan N, Laroze D, Pedraja-Rejas L. An effect of waste discharge concentration and electromagnetic field on chemically reactive Bingham fluid flow with the analysis entropy generation and mass transfer. Hybrid Adv. 2025;8: 100344.
5. Gamaoun KSF, Abdulrahman A, Paramesh SO, Kumar R, et al. Impact of exponential form of internal heat generation on water-based ternary hybrid nanofluid flow by capitalizing non-Fourier heat flux model. Case Stud Therm Eng. 2022;38:102332.
6. Datta-Gupta A, King MJ. A semianalytic approach to tracer flow modeling in heterogeneous permeable media. Adv Water Resour. 1995;18(1):9–24. https://doi.org/10.1016/0309-1708(94)00021-V.
7. Bernard GG, Jacobs WL. Effect of foam on trapped gas saturation and on permeability of porous media to water. Soc Pet Eng J. 1965;5(4):295–300. https://doi.org/10.2118/1204-PA.
8. Akshatha HD, Sachhin SM, Mahabaleshwar US, Lodhi RK, Ramesh K. Dynamics of sodium alginate-based ternary nanofluid flow over a stretching sheet with Al2O3, SiO2, and TiO2 nanoparticles. Multiscale Multidiscip Model Exp Des. 2024;8: 32.
9. Vafai K, Kim SJ. Fluid mechanics of the interface region between a porous medium and a fluid layer—an exact solution. Int J Heat Fluid Flow. 1990;11(3):254–6. https://doi.org/10.1016/0142-727X(90)90045-D.
10. Ochoa-Tapia JA, Whitaker S. Momentum transfer at the boundary between a porous medium and a homogeneous fluid—I. Theoretical development. Int J Heat Mass Transf. 1995;38(14):2635–46. https://doi.org/10.1016/0017-9310(94)00346-W.
11. Haga JB, Osnes H, Langtangen HP. On the causes of pressure oscillations in low-permeable and low-compressible porous media. Int J Numer Anal Methods Geomech. 2012;36(12):1507–22. https://doi.org/10.1002/nag.1062.
12. Choi SUS, Eastman J. Enhancing thermal conductivity of fluids with nanoparticles. Presented at: Proceedings of the ASME International Mechanical Engineering Congress and Exposition; 1995.
13. Huminic G, Huminic A. The heat transfer performances and entropy generation analysis of hybrid nanofluids in a flattened tube. Int J Heat Mass Transf. 2018;119:813–27. https://doi.org/10.1016/j.ijheatmasstransfer.2017.11.155.
14. Das PK. A review based on the effect and mechanism of thermal conductivity of normal nanofluids and hybrid nanofluids. J Mol Liq. 2017;240:420–46. https://doi.org/10.1016/j.molliq.2017.05.071.
15. Suresh S, Venkitaraj KP, Hameed MS, Sarangan J. Turbulent heat transfer and pressure drop characteristics of dilute water based Al_2O_3–Cu hybrid nanofluids. J Nanosci Nanotechnol. 2014;14(3):2563–72. https://doi.org/10.1166/jnn.2014.8467.
16. Siddiqui FR, Tso CY, Chan KC, Fu SC, Chao CYH. On trade-off for dispersion stability and thermal transport of Cu–Al_2O_3 hybrid nanofluid for various mixing ratios. Int J Heat Mass Transf. 2019;132:1200–16. https://doi.org/10.1016/j.ijheatmasstransfer.2018.12.094.
17. Sachhin SM, Mahabaleshwar US. Bioconvection impact on chemically reactive Prandtl-Eyring nanofluid flow through Darcy-Forchheimer media based on Buongiorno's framework. Phys Fluids. 2025;37:063124.
18. Rostami S, Toghraie D, Shabani B, Sina N, Barnoon P. Measurement of the thermal conductivity of MWCNT–CuO/water hybrid nanofluid using artificial neural networks (ANNs). J Therm Anal Calorim. 2021;143(2):1097–105. https://doi.org/10.1007/s10973-020-09458-5.

19. Nisa ZU, et al. A novel fractional study on free convection flow of Brinkmann hybrid nanofluid over an inclined plate. Therm Sci. 2022;26:229–37.
20. Sene N. Analytical investigations of the fractional free convection flow of Brinkman type fluid described by the Caputo fractional derivative. Results Phys. 2022;37: 105555. https://doi.org/10.1016/j.rinp.2022.105555.
21. Meften GA, Ali AH, Al-Ghafri KS, Awrejcewicz J, Bazighifan O. Nonlinear stability and linear instability of double-diffusive convection in a rotating with LTNE effects and symmetric properties: brinkmann-forchheimer model. Symmetry. 2022;14(3): 565. https://doi.org/10.3390/sym14030565.
22. El-Sapa S, Almoneef AA. The axisymmetric migration of an aerosol particle embedded in a Brinkmann medium of a couple stress fluid with slip regime. Eur J Pure Appl Math. 2022;15(4):4549. https://doi.org/10.29020/nybg.ejpam.v15i4.4549.
23. Sachhin SM, Granados-Ortiz F-J, Mahabaleshwar US, Ortega-Casanova J, Pérez LM. Heat and mass transfer analysis of a Bingham ternary nanofluid exposed to radiation over stretching/shrinking sheets and Stefan blowing effect. Alexandria Eng J. 2025;129:515–29.
24. Wang Z, Liu W, Huang J. Modeling and numerical analysis of compressible Darcy-Brinkman fluid flow in fractured media with finite volume method on non-matching grids. J Comput Appl Math. 2023;420: 114774. https://doi.org/10.1016/j.cam.2022.114774.
25. Devi M, Gupta U. Stability analysis of binary Casson nanofluid convection with viscosity and conductivity variations using Darcy-Brinkman model. J Heat Transfer. 2022;144: 121201. https://doi.org/10.1115/1.4055675.
26. Hamid M, Usman M, Khan ZH, Ahmad R, Wang W. Dual solutions and stability analysis of flow and heat transfer of Casson fluid over a stretching sheet. Phys Lett A. 2019;383(20):2400–8. https://doi.org/10.1016/j.physleta.2019.04.050.
27. Khan U, Zaib A, Ishak A, Roy NC, Bakar SA, Muhammad T, Aty AHA, Yahia IS. Exact solutions for MHD axisymmetric hybrid nanofluid flow and heat transfer over a permeable non-linear radially shrinking/stretching surface with mutual impacts of thermal radiation. Eur Phys J Spec Top. 2022;231:1195–204.
28. Khan KA, Jamil F, Ali J, Khan I, Ahmed N, Andualem M, et al. Analytical simulation of heat and mass transmission in Casson fluid flow across a stretching surface. Math Probl Eng. 2022;2022:5576194.
29. Liu IC. A note on heat and mass transfer for a hydromagnetic flow over a stretching sheet. Int Commun Heat Mass Transf. 2005;32(8):1075–84. https://doi.org/10.1016/j.icheatmasstransfer.2005.02.003.
30. Sachhin SM, Mahabaleshwar US, Swaminathan N, Pérez LM, Wang J. Thermal dynamics and magnetohydrodynamics in ferrofluidic wall jet flow: entropy generation in heat and mass transfer. J Mol Liq. 2025;427:127449.
31. Mane PS, Patil VS, Patil AB, Humane PP, Maharudrappa I, Sankad GC. Study of thermal radiation and dissipation effects on MHD prandtl hybrid nanofluid flow past an exponential stretched porous device. Therm Sci Eng Prog. 2025;62: 103677. https://doi.org/10.1016/j.tsep.2025.103677.
32. Reddy V, Kandasamy J, Sivanandam S. Impacts of Casson model on hybrid nanofluid flow over a moving thin needle with Dufour and Soret and thermal radiation effects. Math Comput Appl. 2022;28: 2. https://doi.org/10.3390/mca28010002.
33. Kalidasan K, Velkennedy LR, Kanna PR. Laminar natural convection of copper–titania/water hybrid nanofluid in an open ended-C-shaped enclosure with an isothermal block. J Mol Liq. 2017;246:251–8.
34. Sarwar N. The application of ternary nanoparticles in heat transfer of an MHD non-Newtonian fluid flow. Micromachines. 2022;18:2149.
35. Takabi B, Saleh S. Augmentation of the heat transfer performance of a sinusoidal corrugated enclosure by employing hybrid nanofluid. Adv Mech Eng. 2014;16: 147059.
36. Crane LJ. Flow past a stretching plate. Z Angew Math Phys ZAMP. 1970;21:645–7.
37. Darcy H. Recherches expérimentales relatives au mouvement de l'eau dans les tuyaux. *Mémoires Présentés par Divers Savants à l'Académie des Sciences de l'Institut Impérial de France.* Paris: Académie des Sciences de l'Institut Impérial de France; 1858. p. 14–401.
38. Navier CLMH. Sur les lois du mouvement des liquides. Mem Acad R Sci Inst Fr. 1827;6:389–440.
39. Souayeh B, Ben-Cheikh N, Ben-Beya B. Numerical simulation of three-dimensional natural convection in a cubic enclosure induced by an isothermally-heated circular cylinder at different inclinations. Int J Therm Sci. 2016;110:325–39.
40. Bezi S, Souayeh B, Ben-Cheikh N, Ben-Beya B. Numerical simulation of entropy generation due to unsteady natural convection in a semi-annular enclosure filled with nanofluid. Int J Heat Mass Transfer. 2018;124:841–59.
41. Hdhiri N, Souayeh B, Alfannakh H, Beya BB. Natural convection study with internal heat generation on heat transfer and fluid flow within a differentially heated square cavity filled with different working fluids and porous media. BioNanoSci. 2019;9:702–22.
42. Souayeh B, Hdhiri N. Mixed convective heat transfer and heat generation simulation in lid-driven enclosure filled with porous medium. Int J Mod Phys C. 2021;32:2150106.
43. Souayeh B, Ben-Cheikh N, Ben-Beya B. Effect of thermal conductivity ratio on flow features and convective heat transfer. Part Sci Technol. 2017;35:565–74.
44. Al Nuwairan M, Hafeez A, Khalid A, Souayeh B, Alfadhli N, Alnaghmosh A. Flow of maxwell fluid with heat transfer through porous medium with thermophoresis particle deposition and Soret–Dufour effects: numerical solution. Coatings. 2022;12:1567.
45. Waseem M, Jawad M, Naeem S, Bognár G, Alballa T, Khalifa HAEW, et al. Regression analysis of Cattaneo-Christov heat and thermal radiation on 3D Darcy flow of non-Newtonian fluids induced by stretchable sheet. Case Stud Therm Eng. 2024;61:104959.
46. Lone SA, Ali F, Saeed A, Bognár G. Irreversibility analysis with hybrid cross nanofluid of stagnation point and radiative flow (TiO2+CuO) based on engine oil past a stretchable sheet. Heliyon. 2023;9: e15056.
47. Awati VB, Goravar A, Mahesh Kumar N, Bognár G. Chemically radiative aspects of mixed convection unsteady MHD stagnation point flow with Williamson nanofluid: semi-numerical approach. Alexandria Eng J. 2025;125:647–62.
48. Lone SA, Anwar S, Saeed A, Bognár G. A stratified flow of a non-Newtonian Casson fluid comprising microorganisms on a stretching sheet with activation energy. Sci Rep. 2023;13:11240.